Nanocrystal-based active photonics device through spatial design of light-matter coupling

Tung Huu Dang, Adrien Khalili, Claire Abadie, Charlie Gréboval, Mariarosa Cavallo, Huichen Zhang, Erwan Bossavit, James K Utterback, Erwan Dandeu, Yoann Prado, et al.

Nanocrystal based Active Photonics Device through Spatial Design of Light-Matter Coupling

Tung Huu Dang[1,2], Adrien Khalili[2], Claire Abadie[2], Charlie Gréboval[2], Mariarosa Cavallo[2], Huichen Zhang[2], Erwan Bossavit[2], James K. Utterback[2], Erwan Dandeu[2], Yoann Prado[2], Gregory Vincent[3], Sandrine Ithurria[4], Yanko Todorov[1], Carlo Sirtori[1], Angela Vasanelli[1*], Emmanuel Lhuillier[2*]

[1] Laboratoire de physique de l'Ecole Normale Supérieure, ENS, Université PSL, CNRS, Sorbonne Université, Université de Paris, 75005 Paris, France
[2] Sorbonne Université, CNRS, Institut des NanoSciences de Paris, INSP, 75005 Paris, France.
[3] ONERA - The French Aerospace Lab, 6, chemin de la Vauve aux Granges, BP 80100, 91123 Palaiseau, France.
[4] Laboratoire de Physique et d'Etude des Matériaux, ESPCI-Paris, PSL Research University, Sorbonne Université UPMC Univ Paris 06, CNRS, 10 rue Vauquelin 75005 Paris, France.

Abstract: Integration of photonic structures in nanocrystal-based photodetectors has been demonstrated to improve device performances. Furthermore, bias-dependent photoresponse can be observed in such devices as a result of the interplay between hopping transport and inhomogeneous electromagnetic field. Here, we investigate the main physical concepts leading to a voltage-dependent photoresponse. We first bring evidence of bias-dependent carrier mobilities in a nanocrystal array over a wide range of temperatures. Then, we realize an infrared sensing device using HgTe nanocrystals, where the electrodes also play the role of a grating, inducing a spatially inhomogeneous absorption. The obtained device exhibits a significant bias-dependent photoresponse while possessing a competitive detection performance in the extended short-wave and mid-wave infrared, with detectivity reaching 7×10^{10} Jones at 80 K and a fast response time of around 70 ns. This work provides the foundation for further advancements in nanocrystal-based-active photonics devices.

Keywords: nanocrystals, carrier mobility, infrared, active photonics, light matter coupling.

*To whom correspondence should be sent: angela.vasanelli@ens.fr and el@insp.upmc.fr

INTRODUCTION

Nanocrystals (NCs) present broadly tunable optical features, from visible to infrared range.[1] Compared to epitaxially grown materials, their colloidal synthesis releases the constraint of being epitaxially matched to a substrate. This eases the growth process as well as the coupling to read-out circuit for the design of focal plane arrays.[2–5] However, infrared sensors based on nanocrystals keep suffering from a low carrier diffusion length, which makes charge collection inefficient for devices whose electrode separation is significantly larger than the diffusion length.[6] The resulting thin films are thus poorly photoresponsive, and light management strategies have to be introduced to absorb a significant part of the incident light into a NC slab whose size matches the diffusion length. In diodes based on vertical transport, absorption enhancement can be obtained by employing Fabry-Perot cavities.[7,8] More advanced geometries have been proposed to harness the coupling with light,[9] including plasmonic cavities,[10–15] guided mode resonators,[16–19] Fabry-Perot resonators,[20] metal-insulator-metal patches,[21–23] metasurfaces[24,25], as well as combinations of these light resonators. By introducing the resonators, the absorption spectrum of the device can be reshaped with respect to that of the absorbing NCs. Absorption enhancement and spectral modification induced by a photonic structure are phenomena that are quite generally observed in semiconductor systems coupled to resonators or metasurfaces. Beyond these phenomena, another cavity-induced effect can be observed in NC-based devices, activated by the transport mechanisms peculiar to NC films. In a device consisting of a NC film coupled to a photonic structure, Dang *et al.*[21] observed a 15 meV blue shift of the photocurrent peak, fully reversible under bias application. The authors demonstrated that the photonic structure induces an inhomogeneous absorption within the NC film, and then the bias dependence of the charge collection tunes the spectral shape of the photoresponse. Even though the observed spectral shift was only 5% of the exciton peak linewidth, the possibility of using nanocrystals as materials for active nanophotonics[26] is very interesting, in a field dominated by MEMS[27] and phase change materials[28,29].

In this work, we investigate the different mechanisms that govern bias reconfigurability of a NC-based device, and we propose a detector showing a strong bias-dependent photoresponse. In order to design such a device, two different properties have been controlled: carrier transport and light absorption. Concerning carrier transport, hopping conduction enables a transport diffusion length far below the device size. As a result, charge collection is more efficient in the vicinity of the electrodes. Here, we bring solid evidence of the bias dependence of the carrier mobility and thus of the diffusion length. The consequence of this observation is that bias can be used as a knob to tune the device's active area. On the other hand, the absorbance of the device is spatially engineered through the use of a photonic structure. We show that, by coupling these two properties, we can use the bias dependence of the diffusion length to obtain a bias reconfigurable infrared sensor operating up to 240 K. Compared to previous work[21] (only spectral shift was observed and only up to 120 K), we demonstrate a far more significant spectral reconfigurability now compatible with relative amplitude modification of the optical resonances separated over an extended spectral window. Moreover, it is worth stressing that this result has been obtained in a device with simple architecture, by carefully engineering the size and periodicity of interdigitated electrodes on glass.

RESULTS AND DISCUSSION

Because the bias dependence of the carrier diffusion length is a central element in the design of bias reconfigurable photoresponse, we first study the effect of an electrostatic field on effective carrier mobilities in the nanocrystal arrays. On a Si/SiO_2 substrate, we build a field-effect transistor (FET) whose conductive channel comprises HgTe nanocrystal arrays.[30] A scheme of the FET device is indicated in figure S 2a with the nanocrystal film thickness of around 180 nm. The nanocrystals are synthesized using the Prado *et al.* procedure.[31] The obtained particles present a spherical shape with a typical size of 8 nm, see **Figure 1a** and S 1. The absorption spectrum of the NC solution

shows a clear excitonic absorption around 3600 cm^{-1} (≈2.8 µm), along with a doublet around 2900 cm^{-1} due to the presence of capping ligands, see **Figure 1a**. Phase transfer is then performed [32,33] to exchange the initial long capping ligands for hybrid passivation combining short thiols and ions. Then smooth, conductive NC films are prepared by spin-coating, see *Device Fabrication* in *Supporting Information*. **Figure 1b** shows the FET transfer curve at 120 K. The NC film appears to be quasi-intrinsic with a minimum of conductance close to zero gate bias, and the transfer curve exhibits an ambipolar behavior with both hole (under negative gate bias) and electron (under positive gate bias) conduction regimes. At high gate voltages, a decrease of the drain-source current is observed, which is the characteristic of Pauli blocking at high electronic density.[33–35] As the temperature increases, the transfer curve shifts towards the negative side, indicating a *n*-doped film, see Figure S 3. As our FET operates in the linear regime (Figure S 2b), field-effect carrier mobilities are extracted using the linear region, for a source-drain voltage V_{DS} negligible with respect to the gate voltage V_{GS}. In this regime, the mobility can be extracted as: $\mu = \frac{L}{W.C_i.V_{DS}} \times \frac{\partial I_{DS}}{\partial V_{GS}}$ where L is the channel length, W is the channel width, C_i is gate insulator capacitance per unit area (here, C_i=11 nF.cm^{-2} for a 300 nm SiO_2 layer), I_{DS} is the drain-source current. Noticeably, we observe an increase in both electron and hole mobilities under applied source-drain electric field. At 120 K, electron mobility presents a 4-fold increase from 0.013 $cm^2\ V^{-1}\ s^{-1}$ to 0.054 $cm^2\ V^{-1}\ s^{-1}$ when the drain-source bias is increased from 0.2 V to 2 V. On the same range of bias voltage, hole mobility shows an even more significant increase with a 26-fold increase from 6.2x10^{-4} $cm^2\ V^{-1}\ s^{-1}$ to 0.016 $cm^2\ V^{-1}\ s^{-1}$, see **Figure 1c**.

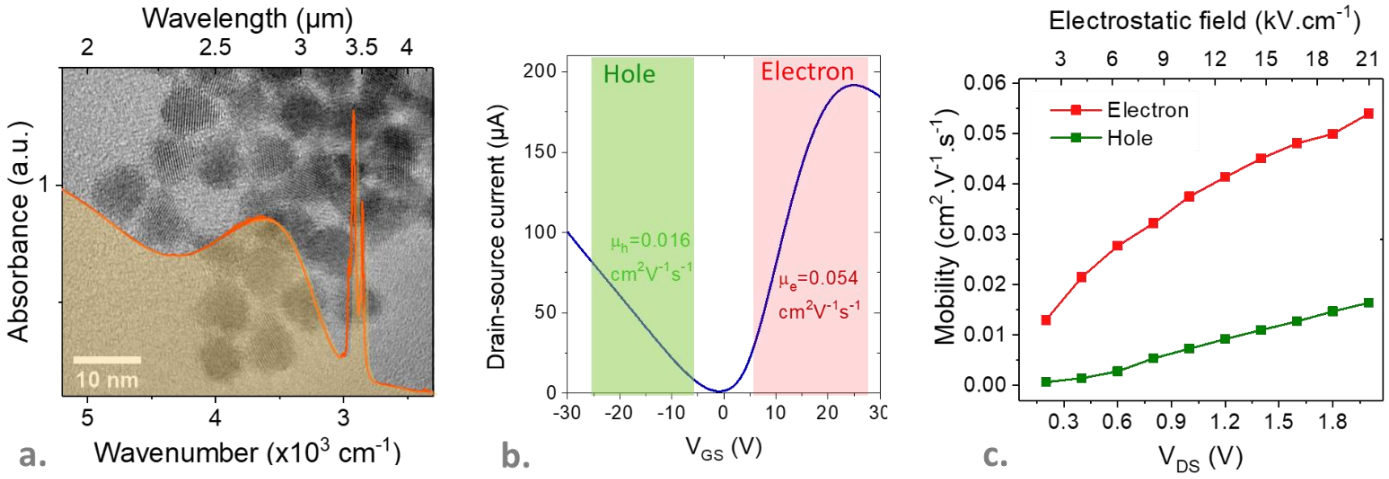

Figure 1. HgTe nanocrystals and effect of electrostatic field on carrier transport. *a. Room-temperature absorption spectrum of the HgTe NCs in solution. The background is a high-resolution transmission electron microscopy image of the HgTe NCs. b. FET transfer curve as a function of gate potential when a bias of 2 V is applied between the drain and source electrodes, at 120 K. c. Electron and hole mobilities as a function of drain-source bias at 120 K.*

The bias-dependence of mobility is observed from 120 K to 240 K, see Figure S 4. This increase of carrier mobility under applied electric field is rather significant. Nenashev *et al.*, considering a hopping system with Miller-Abraham transition rates and Gaussian disorder model, show that $\mu(F)$, while solely depending on charge carrier localization length, can be strongly enhanced under applied electric field.[36] More recently, Xing *et al.* suggest that the presence of positional disorder may enhance carrier mobility by enabling pathways across the NC film.[37] However, they anticipate that

the carrier residence time on the NCs remains the same while only a slight increase of carrier mobilities with electric field should be expected, contrary to our observation.

An increase of carrier mobility with increasing bias implies an increased carrier diffusion length (L_D), assuming that the carrier lifetime τ remains mostly unaffected by electric field application. The Einstein relation links the diffusion coefficient D to the carrier mobility μ through $D= \mu k_B T/e$, with k_B the Boltzmann constant, e the elementary charge, and T the temperature. This leads to $L_D=(D.\tau)^{1/2}=(\mu k_B T/(e.\tau))^{1/2}$, and thus the 4 and 26-fold increase in mobility with bias in the range of our experiment corresponds to 2 and 5-fold increase of the carrier diffusion lengths for electrons and holes, respectively.

In the following, we exploit the electric field dependence of the mobility to build a HgTe NC-based-photodetector allowing configurable photo-response. Indeed, the bias applied to the photodetector modifies the value of the diffusion length, which in turn affects the spatial extent of the active region from which photoexcited carriers are collected. This gives rise to a reconfigurable response device if the absorption of the NC film is inhomogeneous.[21] In order to implement a spatially inhomogeneous absorption, the NC array is coupled to a grating resonator which has a dual role of collecting photoexcited carriers and generating multiple absorption resonances.

The geometry of our detector is depicted in **Figure 2a**. Despite being a simple geometry, the grating coupled to the nanocrystal film offers several degrees of freedom for the design of the light-matter coupling (*i.e.,* the grating period *p*, the electrode size *s*, and the film thickness t_{NC}). On a glass substrate, we fabricate the gold grating using electron beam lithography before functionalizing the structure with a film of HgTe NCs for photodetection in the short and mid-wave infrared. The design is guided by finite element method simulations, see *Finite element method simulation and design of the device* in *Supporting Information*.

Our objective is to design at least two electromagnetic modes: one located in the vicinity of the electrodes in order for generated photocarriers to be collected under low applied electric fields, while the other one is located away from the electrodes to generate photocarriers that will only be collected under higher electric fields. The latter mode is designed by taking advantage of the impedance mismatch between the NC film in the openings between the electrodes and the ones on the top of the gold. Under TE polarization, a Fabry-Perot (FP) resonance, spatially located between the electrodes, can be generated as long as the gold and NC film thicknesses are well-chosen, see **Figure 2c** and S6-7**.** The resonance wavelength of this mode is driven by the opening size $o = p\text{-}s = 2.n_{eff}.\lambda_{FP}$, where n_{eff} is the effective index of the mode. Here, this resonance is also matched with the NC exciton, with a peak around 3.1 µm, as shown in the absorption spectrum in **Figure 2b**. We then design the mode located nearby the electrodes. Thanks to the presence of the grating, incoming light can be coupled with a waveguide mode.[16–18,38] By carefully choosing the grating period *p*, diffraction orders in the NC layer can couple to a guided mode, referred to as a guided-mode resonance (GMR). More importantly, the GMR focuses light on the NCs above the grating stripes and features a resonant peak around 2.2 µm, see **Figure 2d**. The nature of the GMR is revealed by its dispersive character, see the dispersion maps in Figure S8. Detailed analysis and calculations on the GMR can be found in Figure S5-S8. With the two modes designed to be separated spectrally and spatially, we hence expect to see bias reconfigurability when the device is illuminated under TE polarization. Let us now discuss the resonance around 2.5 µm in TM polarization in **Figure 2b**. This resonance, referred to as TM cavity resonance, strongly enhances the electromagnetic field and absorption of the NC film above the electrodes, see **Figure 2e** and Figure S10a. One can also notice a feature at around 3 µm that corresponds to the nanocrystal band edge after ligand exchange. Expectedly, the simulated NC absorption in the slits is negligible,

see our simulated spectra in Figure S10b. Therefore, a negligible voltage dependence is anticipated for the device photoresponse under TM polarization. A comparison of electric field distributions for the TE and TM resonances is presented in figure S12 along with color maps shown in figure S6 and S10.

The set of geometrical parameters used for fabrication of the grating corresponds to a grating period *p* and stripe size *s* of 1.6 µm and 0.95 µm, respectively, see Figure S14-15 for microscopy images, while the HgTe film has a thickness of around 270 nm. **Figure 2b** compares simulated NC absorption spectra with the measured device's photoresponse. Under both TE and TM polarizations, the experimental and simulated spectra show an excellent agreement in the targeted range from 1.5 µm to 4.0 µm.

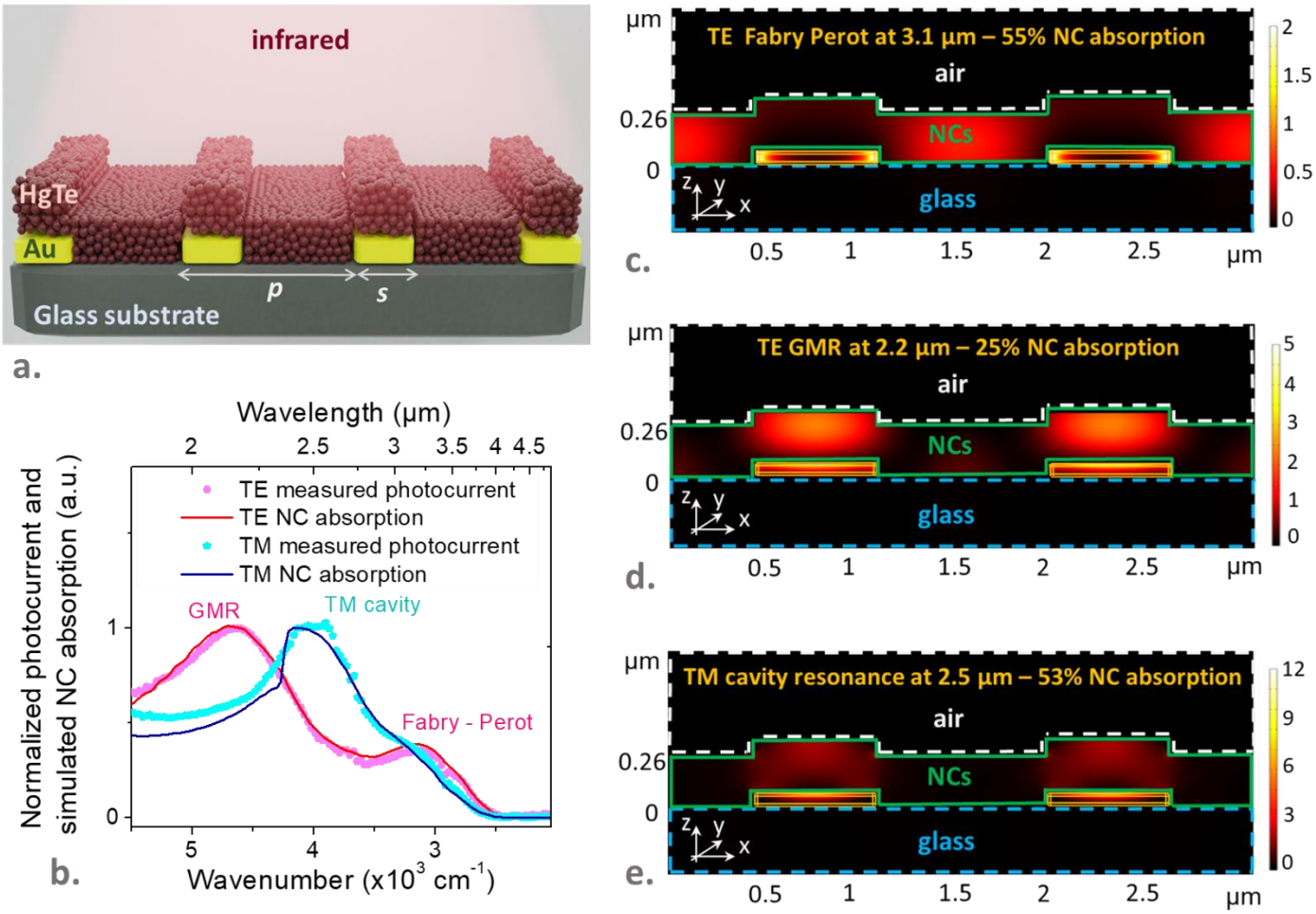

Figure 2. Design of the infrared sensor based on HgTe NCs. *a. Illustration of the HgTe NC infrared detector with grating geometry on a glass substrate. Optical properties of the device are defined by grating period p and stripe size s. b. Comparison of the normalized photocurrent spectra and simulated NC absorption spectra under transverse electric and transverse magnetic polarizations. Here, TE and TM photocurrent spectra of the device are measured at 80 K and under 1.2 V and 0.2 V bias voltages, respectively. For unnormalized spectra, see Figure S 20c. c. (resp. d) Absorption map associated with the Fabry – Perot resonance (resp. GMR resonance) around 3.1 µm (resp. 2.5 µm) in TE polarization (TE – electric field component in the y direction). e. Absorption map associated with the resonance around 2.5 µm in TM polarization (TM - magnetic field component in the y direction).*

.

Figure 3a and **Figure 3b** show the normalized photocurrent spectra of the device as a function of various bias voltages at 80 K. As expected, an apparent tunable photo-response with applied bias can be observed under TE polarization. In contrast, no significant change of the photocurrent spectrum is observed when the incident light is TM polarized. As the applied bias increases, the ratio between the intensity of the TE Fabry-Perot resonance and the intensity of the GMR grows from 0.1 for a bias of 0.1 V to 0.44 for a bias of 1.5 V. Note that this spectral modulation is fully reversible (*i.e.,* the peak intensity ratio decreases when the applied bias decreases) and is not dependent on the bias polarity. Here, Stark effect can be excluded as a possible mechanism to explain the origin of this bias reconfigurability since it requires an electric field above 100 kV.cm^{-1} to generate a much smaller band edge shift,[6,21] also see Figure S20. Moreover, Stark effect will affect both polarizations the same way.

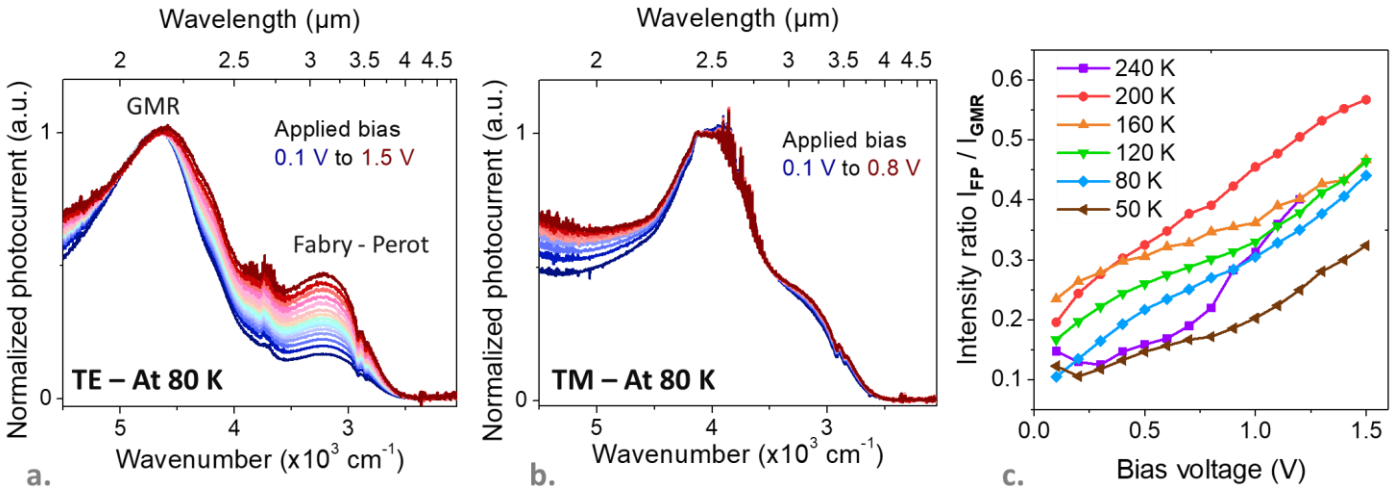

Figure 3. Bias tunability of the device. *a. Photocurrent spectra of the device in TE polarization under various applied biases from 0.1 V to 1.5 V (step of 0.1 V), at 80 K. b. Photocurrent spectra of the device in TE polarization under various applied biases from 0.1 V to 0.8 V (step of 0.1 V), at 80 K. c. Intensity ratio between the Fabry-Perot resonance and the GMR in TE polarization as a function of applied bias at various temperatures.*

The bias dependence of the spectral response of our device under TE polarization is observed in a wide range of temperatures from 50 K to 240 K, see **Figure 3c** and Figure S17, while the shape of TM photocurrent spectrum remains almost unchanged, see Figure S19. Compared to previous work,[21] it should be pointed out that spectral change is far more dramatic. Furthermore, we are able to induce relative photocurrent magnitude reconfiguration, while before, only a small spectral shift was observed. In addition, the careful engineering of the absorption allows observing the effect over a much broader range of temperatures (up to 240 K) compared to 120 K in the previous device.

To this point, it should be noted that the intensity ratio of the two TE resonances increases when photocurrent signal from both resonances also increases with the applied bias, see Figure S16 and S18. We attribute this modulation to different degrees of overlap between electromagnetic resonances and the induced electrostatic field. Since the grating is used as interdigitated electrodes, the in-plane electric field component dominates, and a greater field strength is established in the slits between neighboring electrodes, see Figure S11. Under low electric fields, charge collection mainly occurs near the electrodes, which favors the spectral weight of the nearby resonance, evidenced by a stronger spectral weight of the GMR in **Figure 3a.** When a large electric field is

applied, charge collection becomes more efficient, and the spectral weight associated with the TE Fabry-Perot resonance, spatially localized away from the electrodes, increases.

The drastic change in intensity ratio also raises a crucial point in the design of NC-based infrared sensor, which so far has been mainly focused on enhancing material absorption using optical resonators. In fact, it shows that spatially designing the resonances well aligned with the applied electrostatic field is also essential for efficient charge extraction, meaning that the optical modes can be effectively exploited. However, it is noteworthy that although TE Fabry-Perot resonance field (**Figure 2c)** fits better with electrostatic field map (Figure S 11a) than for TE GMR resonance (**Figure 2d**), photocurrent is higher at GMR resonance because field enhancement is higher.

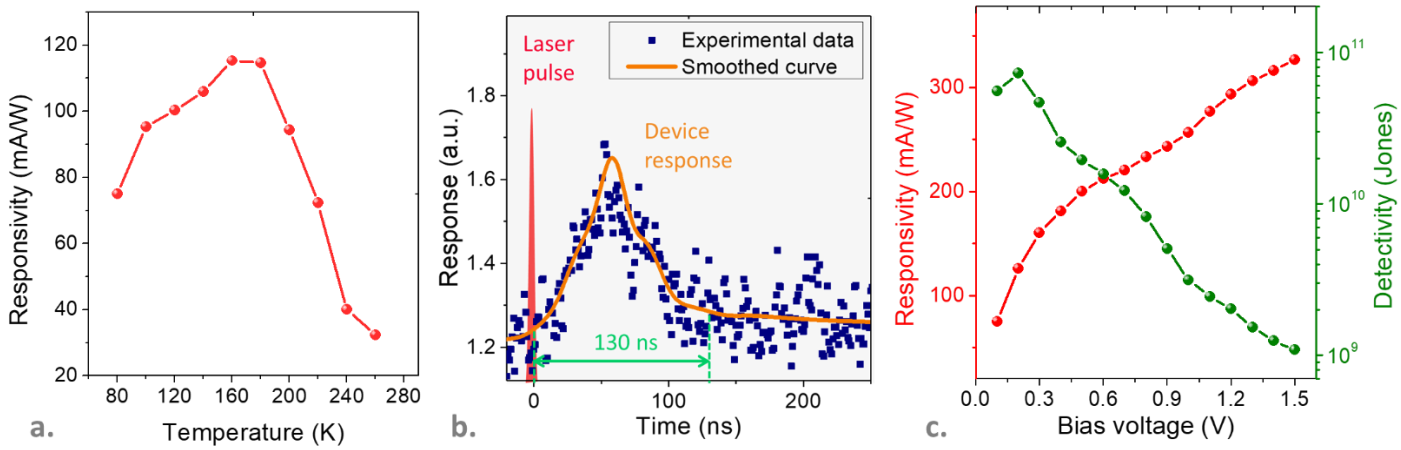

Figure 4. Photodetection performance. *a. Responsivity of the device under broadband illumination (blackbody at 980 ºC) as a function of the temperature when biased with 0.1 V. b. Photoresponse of the device when illuminated with 1.2 ns laser pulses (λ = 1.57 µm), at 80 K. c. Responsivity of the device under broadband illumination (blackbody at 980 ºC) and detectivity (at 1 kHz) of the device as a function of the applied bias, at 80 K.*

The photodetection performance of the device is then characterized. The responsivity under broadband radiation (blackbody at 980 ºC) appears to depend strongly on the temperature. The measured responsivity of the device reaches a maximum of ≈ 110 $mA.W^{-1}$ at around 160 K to 180 K when a bias of 0.1 V is applied, see **Figure 4a**. Noticeably, we observe a significant decrease of responsivity when the temperature goes higher than 200 K for a series of devices fabricated using the same material. This decrease can be attributed to the electron mobility drop above 200 K, as shown in Figure S 4. Fitting the dark current-temperature dependence to the Arrhenius equation gives estimated activation energy of around 150 meV, close to half of the material band-edge energy (≈180 meV), see Figure S 21a. The dark current thus drastically reduces upon cooling. The I-V curve under dark condition is linear at 280 K, and appears more super-linear at low temperatures, see Figure S 21b. A typical transient response of the device to 1.2 ns laser pulse using 1.57 µm laser source is shown in **Figure 4b**, where a quick increase in the photocurrent is followed by a slower drop to the dark current values. The rise time is around 60 ns while and the decay process is estimated to be around 70 ns. For photoconductive devices, signal-to-noise ratio of the detectors improves at low temperatures thanks to the reduction of dark current. At 80 K, *1/f* noise prevails in the noise spectrum of our device, see Figure S22. **Figure 4c** presents the responsivity and detectivity (at 1 kHz) of the device operating at 80 K as functions of the applied bias. The responsivity increases monotonically from 70 $mA.W^{-1}$ to 320 $mA.W^{-1}$ when the bias increases from 0.1 V to 1.5 V. On the other hand, the detectivity peaks at $7x10^{10}$ Jones for 0.2 V applied bias before steadily lowering while maintaining a value of more than 10^9 Jones up to 1.5 V. Table 1 compares

performances of recently developed HgTe NCs-based photodetectors, including our device. Our device, while can be straightforward for fabrication process thanks to the basic geometry design, presents a shorter response time compared to the reported mid-wave infrared detectors while retaining a highly competitive detectivity at low-temperature operation.

Table 1 *: Figures of merit for HgTe NCs sensors with designed light-matter coupling.*

** reported values is setup-limited*

Material	Device design	Spectral range/Cut-off wavelength	Responsivity (mA/W)	Time response	D* (Jones)	Operating Temperature (K)	References
HgTe CdSe	Gate switchable photoresponse	Visible/SWIR 2.5 µm	0.17	-	-	300	[39]
HgTe	Coupling to plasmon	MWIR 4-5 µm	190	-	$1.52x10^{10}$	80	[11]
HgTe	Plasmon+ Fabry-Perot	MWIR 4.5-5 µm	1620	-	$4x10^{11}$	85	[10]
HgTe	Fabry-Perot	SWIR 2.2 µm	500	260 ns	$7.5x10^{10}$	300	[7]
HgTe	Dual band stacked photodiode	SWIR/MWIR 4-5 µm	400	2.5 µs*	$3x10^{11}$	85	[40]
HgTe	Coupling to cavity to achieve 64 narrow bands	SWIR 2.08 µm	200	120 ns	10^{10}	295	[20]
HgTe	Coupling to plasmon	SWIR 2.3 µm	23	-	$3.2x10^{6}$	300	[13]
HgTe PbS	Guided mode resonator	SWIR and extended SWIR 3 µm	1000	-	10^{10}	200	[18]
HgTe	Bias shiftable photoresponse	MWIR 3.5-4 µm	60	5 µs*	$8x10^{9}$	80	[21]
HgTe	3 resonances induced by GMR	SWIR 3 µm	-	14 µs*	10^{12}	30	[16]
HgSe/HgTe	Intraband photodiode	MWIR/SWIR 5 µm	5	500 ns	$1.5x10^{9}$	80	[41]
HgSe/HgTe	Spray - stencil fabricated photodiode	MWIR/SWIR 5 µm	400	6.4 µs	$2x10^{10}$	80	[42]
HgTe	Bias modulated spectral response with basic grating geometry	MWIR 4 µm	320	70 ns	$7x10^{10}$	80	**THIS WORK**

CONCLUSION

To summarize, we bring evidence for bias dependence of carrier mobilities in HgTe nanocrystals film. This property and an inhomogeneous absorption in NC-based devices are critical ingredients for bias-reconfigurable photoresponse in photodetectors. We then fabricated a device using a simple grating geometry, which exhibits a strong tunable photoresponse as a function of bias over a wide range of temperatures from 50 K to 240 K. The significant response tunability can be achieved in our device thanks to the dynamic control of the device's active area with the applied bias. The obtained infrared sensing device also presents a detectivity of $7x10^{10}$ Jones at 80 K and 1 kHz, with

4 μm cut-off wavelength and around 70 ns response time. Our work lays the groundwork for further studies in the field of active photonic systems based on nanocrystals.

METHODS

Chemicals: Mercury chloride ($HgCl_2$, Sigma-Aldrich, 99%), mercury bromide ($HgBr_2$, Alfa Aesar), tellurium powder (Te, Sigma-Aldrich, 99.99%), trioctylphosphine (TOP, Alfa, 90%), oleylamine (OLA, Acros, 80-90%), dodecanethiol (DDT, Sigma-Aldrich, 98%), 2-mercaptoethanol (MPOH, Merck, >99%), and N,N dimethylformamide (DMF, VWR), toluene (VWR, 99.8%) were used. All chemicals were used without further purification, except oleylamine that is centrifuged before use. **Mercury compounds are highly toxic. Handle them with special care.**

1 M TOP:Te precursor: Te powder (2.54 g) was mixed in 20 mL of TOP in a three-neck flask. The flask was kept under vacuum at room temperature for 5 mins, then the temperature was raised to 100 °C. Next, degassing of the flask was conducted for the next 20 mins. The atmosphere was switched to nitrogen, and the temperature was raised to 275 °C. The solution was stirred until a clear orange color was obtained. The flask was cooled to room temperature, and the color changed to yellow. Finally, this solution was transferred to a nitrogen-filled glove box for storage.

HgTe NCs growth: In a 50 mL three-neck flask, 18 mL of oleylamine was degassed under vacuum and heated to 120 °C for one hour. Then, the atmosphere was switched to N_2, and the temperature was set at 120 °C. Meanwhile, in a vial, 72 mg of $HgBr_2$ (0.2 mmol) was dissolved in 1.8 mL of OLA under sonication. After degassing, the solution, 0.2 mL of TOP:Te (1 M), was added (t_w=0). Next, after a waiting time of t_w = 10 mins, the solution was transferred to the syringe, and the content was quickly introduced into hot OLA (120 °C). The solution color quickly turned dark brown. After 3 mins, a cold mixture (*i.e.,* freezer cooled) of 1 mL DDT in 2 mL of toluene was injected, and an ice bath was used to decrease the temperature quickly. The content of the flask was transferred to a centrifuge tube, and QDs were precipitated by adding methanol. After centrifugation, the formed pellet was redispersed in toluene. The solution was precipitated a second time with absolute ethanol and redispersed in toluene. At this step, the QDs were centrifuged in toluene to eliminate the lamellar phase. The solid phase was discarded, and the stable solution phase was transferred to a weighed centrifuge tube and finally precipitated using methanol. Again, the formed pellet (45 mg of dried powder was typically obtained) was redispersed in toluene.

HgTe ink preparation: 20 mg of $HgCl_2$, 2 mL of MPOH, and 18 mL of DMF are mixed to form an exchange solution. 0.25 mL of this exchange solution and 0.5 mL of DMF are added to 0.25 mL of HgTe NCs in toluene. Phase dissociation occurs when a few drops of hexane are added to the mixture: the dark bottom phase is where the NCs migrate while the top transparent phase can be removed with a plastic pipette. This washing step is repeated twice before a few mL of toluene is added, and the mixture is centrifuged at 6000 rpm for 4 minutes. The supernatant is discarded while the formed solid pellets of NCs can be re-dispersed in 100 µL of DMF to obtain the ink of HgTe. A few cycles of sonication – vortex – centrifugation can help to promote particle dispersion.

Spectral photoresponse is measured with a Fisher IS50 FTIR while the sample is biased with a Femto DLPCA 200 amplifier, which is also used for amplifying the photocurrent signal before sending the signal back into the FTIR for spectral analysis. The spectra are typically obtained in continuous scan mode with 4 cm^{-1} resolution and averaged at least 32 times.

Responsivity is measured with at blackbody at 980 ºC as the infrared source. The sample is placed around 24 cm from the blackbody and the incoming flux is modulated by an optical chopper with frequency set to 1000 Hz. A Ge window filtering out all wavelengths shorter than 1.9 µm is placed between the source and the sample. The incident power is then calculated as

$$P(W) = \pi A_{det}.\sin^2\theta/2\,.\cos\varphi.\int_{1.9\mu m}^{\lambda_{cut-off}} \frac{2hc^2}{\lambda^5}\frac{1}{\exp\left(\frac{hc}{\lambda kT}\right)-1}d\lambda$$

where A_{det} is the area of the photodetector, θ is the field of view, φ is the incident angle (typically assumed to be 0º), h is the Planck constant, c is the speed of light, k is Boltzmann constant, T is the blackbody temperature equal to 980 ºC. $\lambda_{cut-off}$ is taken from the absorption edge of the material.

Response time measurement: The photocurrent signal from the sample (inside the cryostat, placed under voltage bias) is amplified with a DUPVA-1-70 amplifier then fed to an oscilloscope. The pulses are generated by a 1573 nm Q-switched pulse laser diode from CNI laser with 100 Hz repetition rate and 1.2 ns pulse duration.

Noise measurement is conducted with a SR780 spectrum analyzer while a device is biased with a Femto DLPCA 200 amplifier. The noise spectra are typically acquired over a frequency from 10 Hz to 1.6 kHz. Typically, the noise current density spectrum is obtained after averaging 100 scans.

Detectivity is computed from $D^* = \frac{\mathcal{R}\sqrt{A}}{S_I}$, where $\mathcal{R}$ is the responsivity of the device, *A* is the device area (*i.e.*, 3.5 x 10^{-4} cm^2), and S_I is the measured noise current density.

Supporting Information

Supporting information includes details relative to (*i*) material characterization, (*ii*) electromagnetic simulation and device design, (*iii*) device fabrication procedure.

COMPETING INTEREST

The authors declare no competing financial interests.

FUNDING SOURCES

The project is supported by ERC starting grants blackQD (grant n° 756225). We acknowledge the use of clean-room facilities at the “Centrale de Proximité Paris-Centre”. This work has been supported by Region Ile-de-France in the framework of DIM Nano-K (grant dopQD). This work was supported by French state funds managed by the ANR within the Investissements d'Avenir programme under reference ANR-11-IDEX-0004-02 and, more specifically, within the framework of the Cluster of Excellence MATISSE and by grants IPER-Nano2 (ANR-18CE30-0023-01), Copin (ANR-19-CE24-0022), Frontal (ANR-19-CE09-0017), Graskop (ANR-19-CE09-0026), NITQuantum (ANR-20-ASTR-0008-01), Bright (ANR-21-CE24-0012-02) and MixDferro (ANR-21-CE09-0029).

REFERENCES

(1) Lu, H.; Carroll, G. M.; Neale, N. R.; Beard, M. C. Infrared Quantum Dots: Progress, Challenges, and Opportunities. *ACS Nano* **2019**, *13*, 939–953.

(2) Rauch, T.; Böberl, M.; Tedde, S. F.; Fürst, J.; Kovalenko, M. V.; Hesser, G.; Lemmer, U.; Heiss, W.; Hayden, O. Near-Infrared Imaging with Quantum-Dot-Sensitized Organic Photodiodes. *Nat. Photonics* **2009**, *3*, 332–336.

(3) Chu, A.; Martinez, B.; Ferré, S.; Noguier, V.; Gréboval, C.; Livache, C.; Qu, J.; Prado, Y.;

Casaretto, N.; Goubet, N.; Cruguel, H.; Dudy, L.; Silly, M. G.; Vincent, G.; Lhuillier, E. HgTe Nanocrystals for SWIR Detection and Their Integration up to the Focal Plane Array. *ACS Appl. Mater. Interfaces* **2019**, *11*, 33116–33123.

(4) J. Ciani, A.; E. Pimpinella, R.; H. Grein, C.; Guyot-Sionnest, P. Colloidal Quantum Dots for Low-Cost MWIR Imaging. In *Infrared Technology and Applications*; 2016; p 981919.

(5) Pejovi, V.; Georgitzikis, E.; Lee, J.; Lieberman, I.; Cheyns, D.; Heremans, P.; Malinowski, P. E. Infrared Colloidal Quantum Dot Image Sensors. *IEEE Trans. Electron Devices* **2021**, *69*, 2840-2850.

(6) Chu, A.; Gréboval, C.; Prado, Y.; Majjad, H.; Delerue, C.; Dayen, J. F.; Vincent, G.; Lhuillier, E. Infrared Photoconduction at the Diffusion Length Limit in HgTe Nanocrystal Arrays. *Nat. Commun.* **2021**, *12*, 1794.

(7) Tang, X.; Ackerman, M. M.; Shen, G.; Guyot-Sionnest, P. Towards Infrared Electronic Eyes: Flexible Colloidal Quantum Dot Photovoltaic Detectors Enhanced by Resonant Cavity. *Small* **2019**, *15*, 1804920.

(8) Ramade, J.; Qu, J.; Chu, A.; Gréboval, C.; Livache, C.; Goubet, N.; Martinez, B.; Vincent, G.; Lhuillier, E. Potential of Colloidal Quantum Dot Based Solar Cells for Near-Infrared Active Detection. *ACS Photonics* **2020**, *7*, 272–278.

(9) Chen, M.; Lu, L.; Yu, H.; Li, C.; Zhao, N. Integration of Colloidal Quantum Dots with Photonic Structures for Optoelectronic and Optical Devices. *Adv. Sci.* **2021**, *8*, 2101560.

(10) Tang, X.; Ackerman, M. M.; Guyot-Sionnest, P. Thermal Imaging with Plasmon Resonance Enhanced HgTe Colloidal Quantum Dot Photovoltaic Devices. *ACS Nano* **2018**, *12*, 7362–7370.

(11) Yifat, Y.; Ackerman, M.; Guyot-Sionnest, P. Mid-IR Colloidal Quantum Dot Detectors Enhanced by Optical Nano-Antennas. *Appl. Phys. Lett.* **2017**, *110,* 041106.

(12) Tang, X.; Wu, G. fu; Lai, K. W. C. Plasmon Resonance Enhanced Colloidal HgSe Quantum Dot Filterless Narrowband Photodetectors for Mid-Wave Infrared. *J. Mater. Chem. C* **2017**, *5*, 362–369.

(13) Zhu, B.; Chen, M.; Zhu, Q.; Zhou, G.; Abdelazim, N. M.; Zhou, W.; Kershaw, S. V; Rogach, A. L.; Zhao, N.; Tsang, H. K. Integrated Plasmonic Infrared Photodetector Based on Colloidal HgTe Quantum Dots. *Adv. Mater. Technol.* **2019**, *4*, 1900354.

(14) Wang, H.; Guo, Y.; Hao, H.; Bian, H.; Aubin, H.; Wei, Y.; Li, H.; Liu, T.; Degiron, A.; Wang, H. Bright CdSe/CdS Quantum Dot Light-Emitting Diodes with Modulated Carrier Dynamics via the Local Kirchhoff Law. *ACS Appl. Mater. Interfaces* **2021**, *13*, 56476–56484.

(15) Wang, H.; Guo, Y.; Zang, J.; Hao, H.; Wang, L.; Liu, T.; Bian, H.; Jiang, R.; Wen, R.; Li, H.; Tong, Y.; Wang, H. Nanoantennas Involved Optical Plasmonic Cavity for Improved Luminescence of Quantum Dots Light-Emitting Diodes. *ACS Appl. Mater. Interfaces* **2021**, *13*, 44760–44767.

(16) Gréboval, C.; Chu, A.; Magalhaes, D. V.; Ramade, J.; Qu, J.; Rastogi, P.; Khalili, A.; Chee, S. S.; Aubin, H.; Vincent, G.; Bals, S.; Delerue, C.; Lhuillier, E. Ferroelectric Gating of Narrow Band-Gap Nanocrystal Arrays with Enhanced Light-Matter Coupling. *ACS Photonics* **2021**, *8*, 259–268.

(17) Rastogi, P.; Chu, A.; Gréboval, C.; Qu, J.; Noumbé, U. N.; Chee, S. S.; Goyal, M.; Khalili, A.; Xu, X. Z.; Cruguel, H.; Ithurria, S.; Gallas, B.; Dayen, J. F.; Dudy, L.; Silly, M. G.; Patriarche, G.; Degiron, A.; Vincent, G.; Lhuillier, E. Pushing Absorption of Perovskite Nanocrystals into the Infrared. *Nano Lett.* **2020**, *20*, 3999–4006.

(18) Chu, A.; Gréboval, C.; Goubet, N.; Martinez, B.; Livache, C.; Qu, J.; Rastogi, P.; Bresciani, F. A.; Prado, Y.; Suffit, S.; Ithurria, S.; Vincent, G.; Lhuillier, E. Near Unity Absorption in Nanocrystal Based Short Wave Infrared Photodetectors Using Guided Mode Resonators. *ACS Photonics* **2019**, *6*, 2553–2561.

(19) Rastogi, P.; Chu, A.; Dang, T. H.; Prado, Y.; Gréboval, C.; Qu, J.; Dabard, C.; Khalili, A.; Dandeu, E.; Fix, B.; Xu, X. Z.; Ithurria, S.; Vincent, G.; Gallas, B.; Lhuillier, E. Complex Optical Index of HgTe Nanocrystal Infrared Thin Films and Its Use for Short Wave Infrared Photodiode

Design. *Adv. Opt. Mater.* **2021**, *9*, 2002066.
(20) Tang, X.; Ackerman, M. M.; Guyot-Sionnest, P. Acquisition of Hyperspectral Data with Colloidal Quantum Dots. *Laser Photonics Rev.* **2019**, *13*, 1900165.
(21) Dang, T. H.; Vasanelli, A.; Todorov, Y.; Sirtori, C.; Prado, Y.; Chu, A.; Gréboval, C.; Khalili, A.; Cruguel, H.; Delerue, C.; Vincent, G.; Lhuillier, E. Bias Tunable Spectral Response of Nanocrystal Array in a Plasmonic Cavity. *Nano Lett.* **2021**, *21*, 6671–6677.
(22) Caligiuri, V.; Palei, M.; Imran, M.; Manna, L.; Krahne, R. Planar Double-Epsilon-Near-Zero Cavities for Spontaneous Emission and Purcell Effect Enhancement. *ACS Photonics* **2018**, *5*, 2287–2294.
(23) Caligiuri, V.; Biff, G.; Palei, M.; Martín-García, B.; Pothuraju, R. D.; Bretonnière, Y.; Krahne, R. Angle and Polarization Selective Spontaneous Emission in Dye-Doped Metal. *Adv. Opt. Mater.* **2020**, 1901215.
(24) Nikola, Đ.; Schwanninger, R.; Yarema, M.; Koep, S.; Yarema, O.; Salamin, Y.; Lassaline, N.; Cheng, B.; Yazdani, N.; Dorodnyy, A.; Fedoryshyn, Y. M.; Wood, V.; Leuthold, J. Metasurface Colloidal Quantum Dot Photodetectors. *ACS Photonics* **2022,** *9*, 482-492.
(25) Caillas, A.; Suffit, S.; Filloux, P.; Lhuillier, E.; Degiron, A. Anomalous Absorption in Arrays of Metallic Nanoparticles: A Powerful Tool for Quantum Dot Optoelectronics. *Nano Lett.* **2022**, 8–13.
(26) Krasnok, A.; Alu, A. Active Nanophotonics. *Proc. IEEE* **2020**, *108*, 628–654.
(27) Stark, T.; Imboden, M.; Kaya, S.; Mertiri, A.; Chang, J.; Erramilli, S.; Bishop, D. MEMS Tunable Mid-Infrared Plasmonic Spectrometer. *ACS Photonics* **2016**, *3*, 14–19.
(28) Shi, X.; Chen, C.; Liu, S.; Li, G. Nonvolatile, Reconfigurable and Narrowband Mid-Infrared Filter Based on Surface Lattice Resonance in Phase-Change Ge2sb2te5. *Nanomaterials* **2020**, *10*, 2530.
(29) Pogrebnyakov, A. V.; Bossard, J. A.; Turpin, J. P.; Musgraves, J. D.; Shin, H. J.; Rivero-Baleine, C.; Podraza, N.; Richardson, K. A.; Werner, D. H.; Mayer, T. S. Reconfigurable Near-IR Metasurface Based on Ge 2 Sb 2 Te 5 Phase-Change Material . *Opt. Mater. Express* **2018**, *8*, 2264.
(30) Gréboval, C.; Chu, A.; Goubet, N.; Livache, C.; Ithurria, S.; Lhuillier, E. Mercury Chalcogenide Quantum Dots : Material Perspective for Device Integration. *Chem. Rev.* **2021**, *121*, 3627–3700.
(31) Prado, Y.; Qu, J.; Gréboval, C.; Dabard, C.; Rastogi, P.; Chu, A.; Khalili, A.; Xu, X. Z.; Delerue, C.; Ithurria, S.; Lhuillier, E. Seeded Growth of HgTe Nanocrystals for Shape Control and Their Use in Narrow Infrared Electroluminescence. *Chem. Mater.* **2021**, *33*, 2054–2061.
(32) Martinez, B.; Ramade, J.; Livache, C.; Goubet, N.; Chu, A.; Gréboval, C.; Qu, J.; Watkins, W. L.; Becerra, L.; Dandeu, E.; Fave, J. L.; Méthivier, C.; Lacaze, E.; Lhuillier, E. HgTe Nanocrystal Inks for Extended Short-Wave Infrared Detection. *Adv. Opt. Mater.* **2019**, *7*, 1900348.
(33) Lan, X.; Chen, M.; Hudson, M. H.; Kamysbayev, V.; Wang, Y.; Guyot-Sionnest, P.; Talapin, D. V. Quantum Dot Solids Showing State-Resolved Band-like Transport. *Nat. Mater.* **2020**, *19*, 323–329.
(34) Hudson, M. H.; Chen, M.; Kamysbayev, V.; Janke, E. M.; Lan, X.; Allan, G.; Delerue, C.; Lee, B.; Guyot-Sionnest, P.; Talapin, D. V. Conduction Band Fine Structure in Colloidal HgTe Quantum Dots. *ACS Nano* **2018**, *12*, 9397–9404.
(35) Yu, D.; Wang, C.; Guyot-Sionnest, P. N-Type Conducting CdSe Nanocrystal Solids. *Science.* **2003**, *300*, 1277–1280.
(36) Nenashev, A. V.; Oelerich, J. O.; Dvurechenskii, A. V.; Gebhard, F.; Baranovskii, S. D. Fundamental Characteristic Length Scale for the Field Dependence of Hopping Charge Transport in Disordered Organic Semiconductors. *Phys. Rev. B* **2017**, *96*, 035204.
(37) Xing, Y.; Yazdani, N.; Lin, W. M. M.; Yarema, M.; Zahn, R.; Wood, V. Effect of Positional Disorders on Charge Transport in Nanocrystal Quantum Dot Thin Films. *ACS Appl. Mater. Interfaces* **2021,** *4*, 631-642.

(38) Wang, S. S.; Magnusson, R. Theory and Applications of Guided-Mode Resonance Filters. *Appl. Opt.* **1993**, *32*, 2606.
(39) Lhuillier, E.; Robin, A.; Ithurria, S.; Aubin, H.; Dubertret, B. Electrolyte-Gated Colloidal Nanoplatelets-Based Phototransistor and Its Use for Bicolor Detection. *Nano Lett.* **2014**, *14*, 2715–2719.
(40) Tang, X.; Ackerman, M. M.; Chen, M.; Guyot-Sionnest, P. Dual-Band Infrared Imaging Using Stacked Colloidal Quantum Dot Photodiodes. *Nat. Photonics* **2019**, *13*, 277–282.
(41) Livache, C.; Martinez, B.; Goubet, N.; Gréboval, C.; Qu, J.; Chu, A.; Royer, S.; Ithurria, S.; Silly, M. G.; Dubertret, B.; Lhuillier, E. A Colloidal Quantum Dot Infrared Photodetector and Its Use for Intraband Detection. *Nat. Commun.* **2019**, *10*, 2125.
(42) Zhang, S.; Chen, M.; Mu, G.; Li, J.; Hao, Q.; Tang, X. Spray-Stencil Lithography Enabled Large-Scale Fabrication of Multispectral Colloidal Quantum-Dot Infrared Detectors. *Adv. Mater. Technol.* **2021**, *2101132*.

TOC graphic

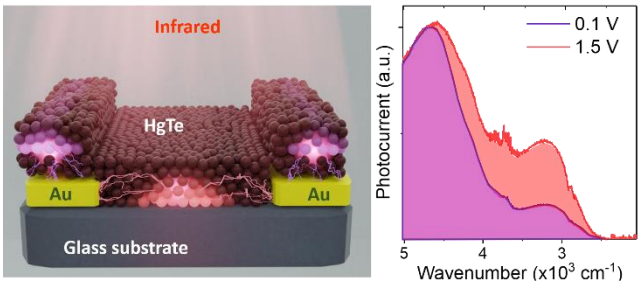
Infrared
HgTe
Au
Au
Glass substrate
0.1 V
1.5 V
Photocurrent (a.u.)
5
4
3
Wavenumber (x10^3 cm^{-1})